Geophysical Research Letters

RESEARCH LETTER
10.1029/2019GL083374

Interactions Between Nonlinear Internal Ocean Waves and the Atmosphere

David G. Ortiz-Suslow[1], Qing Wang[1], John Kalogiros[1,2], Ryan Yamaguchi[1], Tony de Paolo[3], Eric Terrill[3], R. Kipp Shearman[4], Pat Welch[4], and Ivan Savelyev[5]

[1]Department of Meteorology, Naval Postgraduate School, Monterey, CA, USA, [2]National Observatory of Athens, Athens, Greece, [3]Scripps Institution of Oceanography, La Jolla, CA, USA, [4]College of Earth, Ocean, and Atmospheric Sciences, Oregon State University, Corvallis, OR, USA, [5]U.S. Naval Research Laboratory, Washington DC, USA

Key Points:
- The first quantitative analysis detailing interactions between a nonlinear internal ocean wave packet and the atmosphere is presented
- The mean wind velocity and Reynolds stress components responded directly to internal wave-induced roughness variability
- Evidence for responses in the humidity variance and gradient were found, but temperature was not directly impacted by the internal waves

Supporting Information:
- Supporting Information S1

Correspondence to:
Q. Wang,
qwang@nps.edu

Citation:
Ortiz-Suslow, D. G., Wang, Q., Kalogiros, J., Yamaguchi, R., de Paolo, T. & Terrill, E., et al. (2019). Interactions between nonlinear internal ocean waves and the atmosphere. *Geophysical Research Letters*, *46*, 9291–9299. https://doi.org/10.1029/2019GL083374

Received 22 APR 2019
Accepted 9 JUL 2019
Accepted article online 25 JUL 2019
Published online 14 AUG 2019

Abstract The heterogeneity in surface roughness caused by transient, nonlinear internal ocean waves is readily observed in coastal waters. However, the quantifiable impact this heterogeneity has on the marine atmospheric surface layer has not been documented. A comprehensive data set collected from a unique ocean platform provided a novel opportunity to investigate the interaction between this internal ocean process and the atmosphere. Relative to the background atmospheric flow, the presence of internal waves drove wind velocity and stress variance. Furthermore, it is shown that the wind gradient adjusts across individual wave fronts, setting up localized shear that enhanced the air-sea momentum flux over the internal wave packet. This process was largely mechanical, though secondary impacts on the bulk humidity variance and gradient were observed. This study provides the first quantitative analysis of this phenomenon and provides insights into submesoscale air-sea interactions over a transient, internal ocean feature.

Plain Language Summary The ocean surface appears rough because the wind applies a tangential force to the water, which deforms the surface, generating short and steep waves. These small waves, in turn, increase the friction felt by the wind as it blows across the ocean surface, thereby setting up a feedback mechanism that physically links, or couples, the lower atmosphere to the upper ocean. However, our understanding of this interaction in the case of a heterogeneously rough ocean surface is limited. Using a unique ocean platform, we have collected a novel and complete data set demonstrating the impact internal ocean waves have on the near-surface atmospheric variability, through their modulation of the ocean surface roughness. The surface currents associated with internal waves generate bands of smooth and rough water that travel coherently with the internal wave packet. Our analysis shows that these transient surface features have a distinct and profound impact on the physical characteristics and structure of the near-surface atmosphere. In particular, internal waves enhance the wind forcing over the ocean and individual wave fronts significantly alter the vertical wind gradient. Our results provide the first documentation of the impact internal waves have on the atmosphere and suggest that these dynamics should be accounted for when studying fine-scale atmosphere-ocean interactions and the impact internal waves have on the marine environment.

1. Introduction

The tangential wind stress on the ocean surface develops short-gravity and capillary waves that themselves increase the total aerodynamic drag felt by the atmosphere, thereby increasing the stress. This mechanical feedback generates the turbulence within the marine atmospheric surface layer (MASL), facilitating the vertical exchange of momentum and heat across the air-sea interface and forcing the upper ocean boundary layer (UOBL). Thus, the ocean's aerodynamic roughness length, z_0, is codependent on oceanic and atmospheric processes, and while the relationship between wind stress (τ) and z_0 has been accepted (Charnock, 1955), refinements and parameterizations are continually proposed (Drennan et al., 2005; Jiménez & Dudhia, 2018; Kitaigorodskii & Volkov, 1965; MacMahan, 2017). The z_0 complexity hinders the straightforward modeling of the MASL as a wall-bounded shear flow (Prandtl, 1925):

$$U/u* = \frac{1}{\kappa}\log\left(\frac{u_* z}{\nu}\right) + C, \quad (1)$$

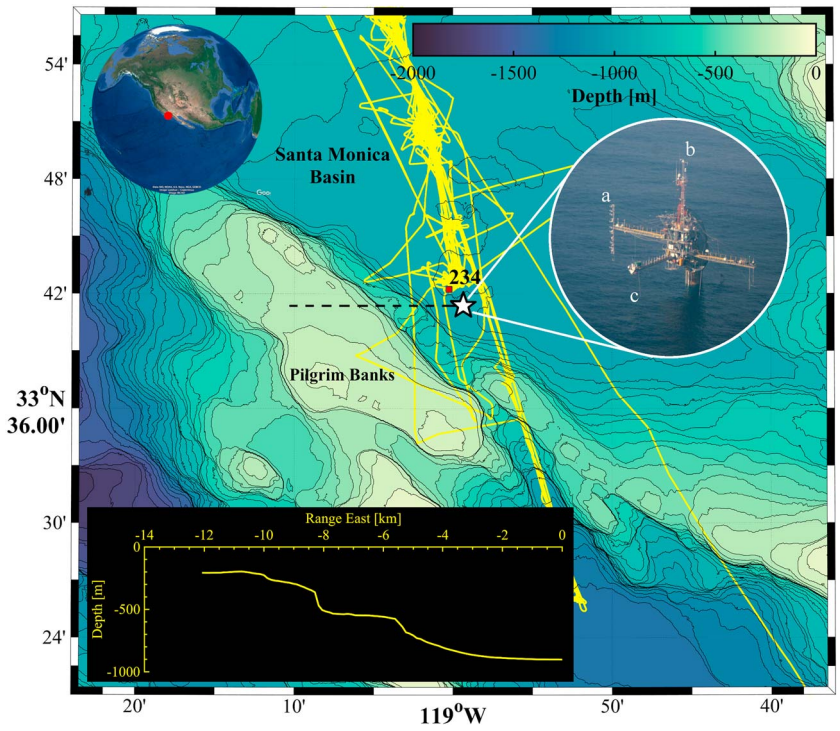

Figure 1. CASPER-West study site, with the mooring location of *FLIP* (star) denoted, on the edge of Pilgrim Banks within the Santa Monica Basin. The yellow line marks the R/V *Sally Ride* ship track—another CASPER-West asset. Inset, relevant *FLIP* measurement systems: (a) micrometeorological mast on the portside boom, (b) X band marine radar on top deck telescoping mast, and (c) thermistor string tethered from the terminus of the face boom (photo credit: D. Khelif, UC Irvine). Also, a cross-section of the depth along a ~14-km transect due west of *FLIP* is provided. Bathymetry data was provided from National Geophysical Data Center, N. (2016). CASPER = Coupled Air Sea Processes and Electromagnetic ducting Research.

where κ is Von Kármán's constant, C is an integration constant, z is height into the constant flux layer, ν is kinematic viscosity, and u_* is the shear velocity ($\tau \equiv \rho u_*^2$). This rare, analytical fluid mechanics solution (Bradshaw & Huang, 1995) presumes the flow and surface are in statistical equilibrium (Hultmark et al., 2013; Jones et al., 2001). Over the ocean, the stress-relevant roughness ($z_0 \propto \nu/u_*$) is primarily carried by gravity capillary waves (Hwang, 2005; Laxague et al., 2015), which have short relaxation times relative to local forcing changes (Zhang et al., 2009).

Various near-surface processes modulate ocean roughness (Woodcock & Wyman, 1947; Zhang et al., 2008), including the convergence-divergence zones associated with oceanic internal waves (Phillips, 1980). In light winds, these zones appear as rough and smooth bands, with the latter phase referred to alternatively as fronts and/or slicks. Nonlinear internal waves (NIWs) are generated by displaced isopycnal surfaces caused by the hydrodynamic (usually tidal) flow over changing bathymetry (Garrett & Munk, 1979). The properties of these high-frequency waves are governed by the Brünt-Väisälä frequency:

$$N^2 = \frac{g}{\rho}\frac{\partial \rho}{\partial z}, \tag{2}$$

where ρ is fluid density and g is the acceleration of gravity. NIWs propagate across large distances, enhancing local transport and turbulence (MacKinnon & Gregg, 2005), until they break on critically steep slopes (Lamb, 2014). The roughness variability due to NIW in the coastal ocean has been observed and conceptualized for decades (Dietz & Lafond, 1950; Ewing, 1950). However, with the advent of synthetic aperture radar technology, the appreciation of the pervasiveness and scale of these NIWs has fundamentally expanded (Apel & Gonzalez, 1983; Brandt et al., 1999; Hsu & Liu, 2000).

A casual ocean observer may perceive smooth-rough banding, but the quantifiable impact NIW-induced roughness has on air-sea interaction remains unknown. While interest in submesoscale air-sea interaction is growing (e.g., Gaube et al., 2019; Wenegrat & Arthur, 2018), the focus has largely been on sea surface

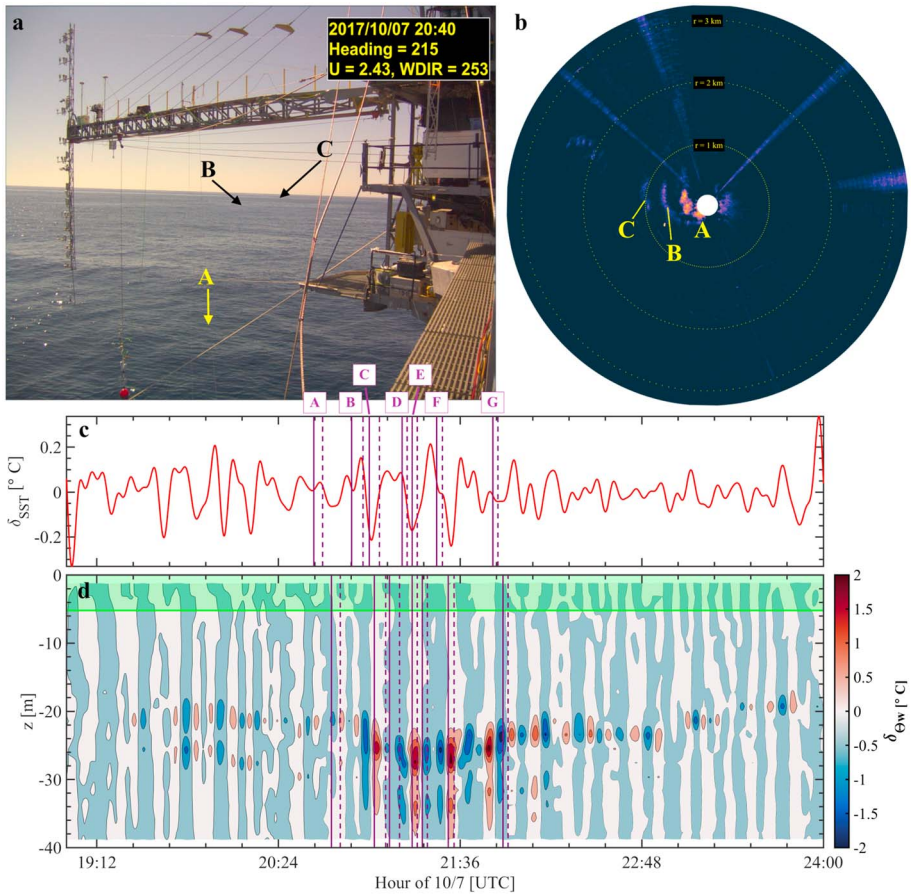

Figure 2. (a) Image from the FC during case study period, *heading* refers to the look direction of the FC, while *U* and *WDIR* refer to mean wind speed and direction (clock-wise from north), respectively, as observed from 3 m above the surface; (b) normalized backscatter intensity map from the WAMOS, acquired 20:38:43 UTC; (c) and (d) show the ocean skin (δ_{SST}) and water temperature (δ_{Θ_w}) anomalies, respectively, from the surface to a depth of 40 m. The identified nonlinear internal wave-associated bands (A–G) are noted in (c) and (d), with select fronts marked in (a) and (b). The vertical solid (dashed) lines mark the arrival of the leading (trailing) edge of the smooth band, as identified in the FC. FC = field camera.

temperature (SST) gradients. The present work is concerned with similar scales but across a transient ocean feature driving mechanical, rather than thermodynamic, heterogeneity. During the Coupled Air Sea Processes and Electromagnetic ducting Research (CASPER) field study, the R/P *FLIP* was deployed and NIWs were consistently observed propagating across the ocean surface. The confluence of an ideal observing platform, UOBL and MASL measurement systems, and favorable environmental conditions provided a unique opportunity to directly evaluate the impact NIWs have on both the mean and turbulent components of the atmosphere.

2. Field Experiment Background

The observations presented here were collected as part of the CASPER west coast field experiment (CASPER-West) conducted offshore of Southern California, within the Santa Monica Basin, from 27 September to 25 October 2017 (Figure 1). CASPER-West sought to characterize MABL variability along a transect running from Point Mugu to the *FLIP* mooring site (~50 km), while simultaneously measuring the oceanic and mesoscale atmospheric environment. This work was the second of two field studies, which aimed to relate environmental forcing to changes in electromagnetic propagation over the ocean (Wang et al., 2018).

2.1. Atmosphere Observations From *FLIP*

The focus here was on the MASL and UOBL measurements collected from *FLIP*, and an abridged summary is provided below; for complete details see Ortiz-Suslow, Wang, et al. (2019).

A heavily instrumented air-sea interaction mast (ASIM) was deployed from *FLIP* on 27 September through 23 October, sampling from 2.5 to 16 m above the mean water level (Figures 1 and 2). The ASIM contained overlapping bulk (X) and perturbation (x) resolving profiles of wind speed (U), air temperature (Θ), and water vapor (Q); *FLIP*'s motion and attitude were measured to correct the raw measurements. Radiometric SST was also measured from *FLIP*'s portside boom. The reader is directed to Ortiz-Suslow, Kalogiros, et al. (2019) for details regarding the measurement systems and quality control of the CASPER-West data.

2.2. Upper Ocean and Surface Measurements

UOBL temperature (Θ_w) structure and ocean surface visualization was used to identify NIWs. The UOBL thermistor string consisted of 20 sensors (RBR *solo,* 2 Hz; vertically spaced every 2 m) and was tethered to the terminus of the face boom (Figures 1 and 2). Absolute depth was determined from a temperature-depth sensor (RBR Duet, 1 Hz) and *FLIP*'s inertial motion data (10 Hz). From Θ_w profiles (not shown here), the string observed a mix layer depth (MLD) ~25 m, but with substantial diurnal oscillation (±10 m). Figure 2 provides contours of temperature anomaly (δ_x), defined as a bandpass filtered (5–17 min) and detrended time series, which were strongest near the MLD.

The ocean surface was visualized using a field camera (FC), as well as an X band marine radar (WAMOS; Figure 1). The FC was particularly well suited to capturing NIW activity near *FLIP* and observed NIW-associated fronts passing underneath the ASIM nearly every day of CASPER-West (see Table 1 in Ortiz-Suslow, Wang, et al., 2019). The WAMOS visualized the ocean surface roughness within a 3-km range of *FLIP* and, after low-pass filtering the backscatter maps, could identify and track NIW fronts. While both systems observe different physical components of NIW-induced roughness, both tools corresponded well (Figure 2).

2.3. Evaluating NIW Impact on the MASL

For this work, NIWs' impact on the MASL was defined as atmospheric variance directly linked to the presence of NIWs, relative to the naturally broadbanded atmospheric state. Two different domains of impact were evaluated:

1. The spectral coherence between NIW and MASL,
2. The quasi-instantaneous response of MASL structure to individual NIW passage.

Conducting a robust analysis of this type requires the confluence of favorable environmental and experimental conditions. Therefore, the focus here will be on one NIW event that occurred during the second half of 7 October.

The spectral analysis (1) was conducted using the auto- (S_{xx}) and covariance ($S_{\overline{xy}}$) power spectrum of the bandpass filtered MASL parameters (cutoffs at 5 and 17 min). These limits were selected because they contained the subtidal peaks in $S_{\Theta_w\Theta_w}$ associated with NIWs. Atmospheric parameters were compared to $S_{\Theta_w\Theta_w}$ from a fixed $z = -27.6$ m (supporting information Figure S1 presents results using $S_{\Theta_w\Theta_w}$ within the mix layer). Only amplitudes with significant coherence (γ^2), between an atmospheric variable and $S_{\Theta_w\Theta_w}$, were analyzed. This was necessary to remove spurious correlation (see Figures S2 and S3); the threshold for significance was set to 95% (χ_{95}) following Biltoft and Pardyjak (2009).

MASL bulk parameters (U, Θ, Q) and turbulent covariances for momentum ($\overline{wu}$, $\overline{wv}$), sensible heat ($\overline{w\theta}$), and latent heat ($\overline{wq}$)—proxies for the interfacial fluxes—were included in the spectral analysis. Here, the three-dimensional perturbation winds are the along- (u), across- (v), and vertical-wind (w) components, respectively. In this convention, $\overline{wu} > 0$ indicated downward momentum flux. θ and q are the temperature and specific humidity in degrees Celsius and grams per kilogram, respectively. Overbars indicate an *appropriate* averaging interval (Δt), which was very short compared to conventional micrometeorological processing, even for typical heterogeneous conditions (Ortiz-Suslow et al., 2015, 2018). Δt was either 60 or 10 s for the spectral or quasi-instantaneous analysis, respectively.

The quasi-instantaneous response (2) was analyzed relative to individual band passage, using non–bandpass filtered data. Here, band and front are used interchangeably and refer to the *visually* identified NIW smooth band. "Quasi" indicates a very short $\Delta t = 10$ s—some averaging is needed to remove high-frequency noise. Here, time will be referenced to the visualized arrival of the band's leading edge at the ASIM. Representative profiles of the approach, arrival, residence, and departure of fronts were produced and analyzed. For this analysis, given observation $\overline{X}(z)$, n profiles from the analysis period were averaged together and normalized

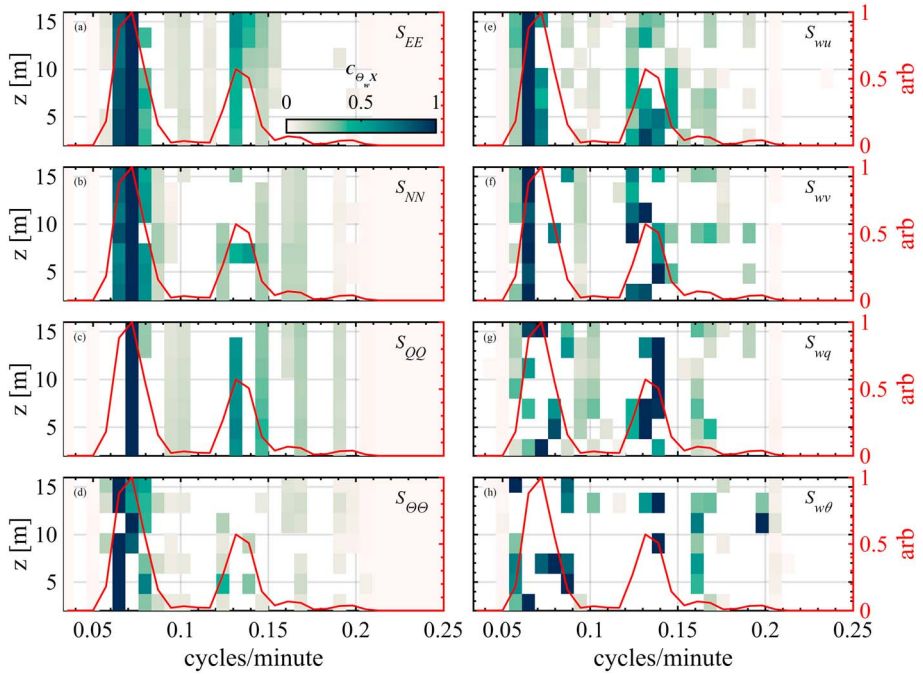

Figure 3. Grids of absolute value, peak-normalized cross-spectral amplitude ($C_{\Theta_w X}$) between MASL parameters (bulk, panels a–d, and turbulent, panels e–h) and Θ_w. $C_{\Theta_w X}$ where $\gamma^2 < \chi_{95}$ have been removed. The peak-normalized $S_{\Theta_w \Theta_w}$ spectrum from $z = -27.6$ m is shown for reference (red line), with peak and subharmonic periods at 13.9 (0.0719 cycles/min) and 7.6 (0.132 cycles/min), respectively. All spectra were calculated over the window 19:00 to 23:30 UTC, 7 October.

by their average peak, $\overline{X}_p$,

$$\overline{X}_c(z) = \frac{\Sigma_i^n \overline{X}_i(z)}{\Sigma_i^n \overline{X}_{p,i}}, \tag{3}$$

where i is summed over n, and using this definition, $\Sigma(X_c) \leq 1$. $\overline{X}_c(z)$ will be compared to a corresponding *control*, which was a normalized mean profile during 01:00–02:00 UTC, 8 October. This hour coincided with the diurnal sea breeze immediately after the case study and presents a period for which the MASL flow was moderate, reasonably stationary and no NIW-associated surface bands were identified. The response of the MASL profiles to individual band passage was assessed relative to these controls (see supporting information and Figures S4–S7 for further details).

3. Results

3.1. NIW Activity Near *FLIP* on 7 October

During this case study, six major NIW fronts (A–G) propagated past *FLIP*, from a west southwesterly direction. Here, "major" indicates a pronounced band easily identifiable in the FC and having cross-frontal widths ~10 m. Major front arrivals were between 20:38 and 21:49 UTC (arrival → time leading edge reaches ASIM). It took about 2–3 min for a front to traverse the ASIM, from which a crude celerity, C_{NIW}, was estimated, ~0.1 m/s.

The visualized band arrivals were synced with Θ_w, to link these surface expressions with UOBL NIW signals. The time lag between the ASIM and thermistor string arrival (~240 s) was estimated assuming a $\Delta x \approx 20$ m and C_{NIW}, for each front's individual arrival/departure times. Front arrival coincided with peaks and troughs at the MLD δ_{Θ_w}, with approximately two fronts per NIW (Figure 2). This corresponds with theoretical expectations, where the phase-locked divergence (convergence) zones should produce alternating smooth (rough) bands (Phillips, 1980). Not every NIW observed from the thermistor string was associated with a corresponding surface front, indicating additional controls on their surface expression.

In addition to these major fronts, at least seven minor fronts were visualized (via FC) between 21:54 and 23:13 UTC. Also, a minor front was observed leading D. These "minor" fronts were significantly narrower

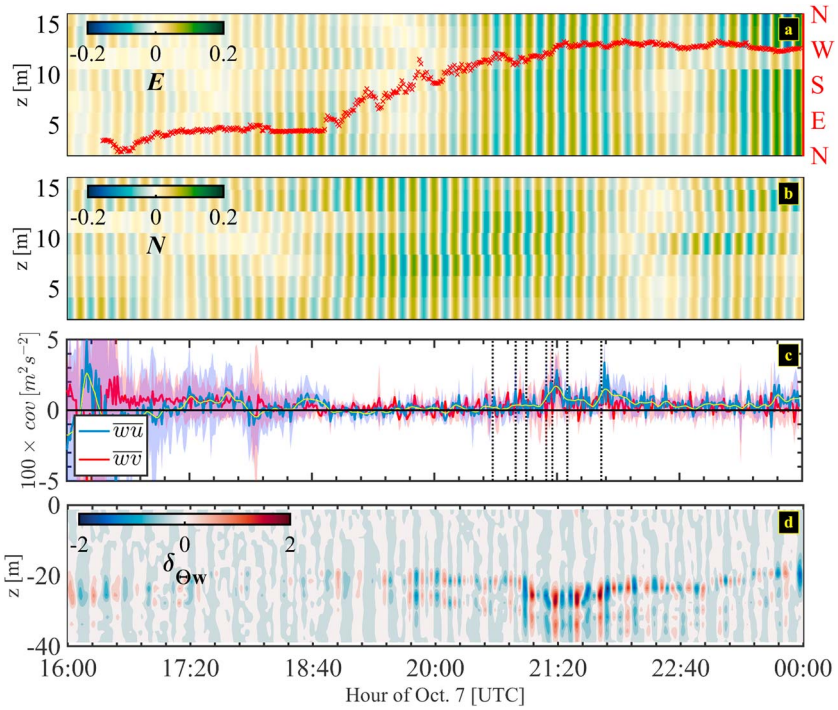

Figure 4. Time-height contours of bandpass filtered (at [13,15] min) anomaly for the eastward (E, panel a) and northward (N, panel b), wind velocities; the red crosses in (a) give the 60-s mean wind direction from $z \sim 5$ m. (c) Vertically averaged $\overline{wu}$ and $\overline{wv}$ (shading spans 2 standard deviations) scaled by 10^2; the yellow line shows the Savitzky-Golay filtered $\overline{wu}$. Vertical lines mark front arrivals A–G. (d) Contour of δ_{Θ_w}.

(< 5 m), of higher frequency, and coincided with diminished NIW activity at the MLD (Figure 2) and the onset of the diurnal see breeze ($U \approx$ 4–5 m/s). It was observed that during this period the tidal flow reversed (westerly to easterly), explaining the reduction in incident NIWs to *FLIP* and potentially some wave-current interaction driving the frequency shift. Due to these confounding factors, particularly the reduced cross-frontal dimension and difficulty with identification, these minor fronts were noted but not analyzed as part of this work.

3.2. Turbulent and Bulk MASL Response to NIW

The NIWs peak and subpeak were at 13.9 and 7.6 min, respectively (Figure 3). All of the MASL covariance spectra revealed some correlation with $S_{\Theta_w\Theta_w}$ at these scales; however, this was varied in strength and with proximity to the surface (see supporting information Figure S7). After filtering $\gamma^2 < \chi_{95}$, only the momentum terms ($S_{\overline{wu},\overline{wv}}$) retained their relationship with the peak $S_{\Theta_w\Theta_w}$ (Figures 3e and 3f). $S_{\overline{wq}}$ exhibited some coherence with the NIW subpeak (Figure 3g), but this result was mixed.

All of the MASL bulk parameters exhibited strong correlations with $S_{\Theta_w\Theta_w}$ at the peak (see supporting information Figure S6). In Figures 3a–3d, it is evident that this persists even after filtering, with the strongest coherence at 13.9 min (the peak) and for the eastward (E) and northward (N) mean winds, as well as Q; also, E and Q were fairly coherent at the subpeak scale (Figures 3a and 3c). The response for Θ was mixed and not as obvious as the other bulk parameters (Figure 3d). In general, MASL-NIW coherence, when evident, was observed throughout the ASIM profile and similar findings were attained when comparing with $S_{\Theta_w\Theta_w}$ from within the mix layer (see supporting information Figure S1). Given the findings in Figure 3, the temporal response of the kinematic MASL variables (E, N, $\overline{wu}$, and $\overline{wv}$) was analyzed to further discern any causal response in the atmosphere due to NIW presence. Here, the analysis window included all of 7 October (only 16:00 to 24:00 UTC given in Figure 4), $\Delta t = 60$ s, and E/N were narrowly filtered at 13 to 15 min—to isolate the response at the $S_{\Theta_w\Theta_w}$ peak. After 18:40, E was approximately cross-frontal and the intensity in the E coincided directly with the arrival, residence, and departure of the NIW packet (Figure 4a). The N component exhibited similar responses, but the signal was confused due to its approximately along-front orientation. Both along- and across-wind momentum flux components (height averaged) revealed a net positive trend

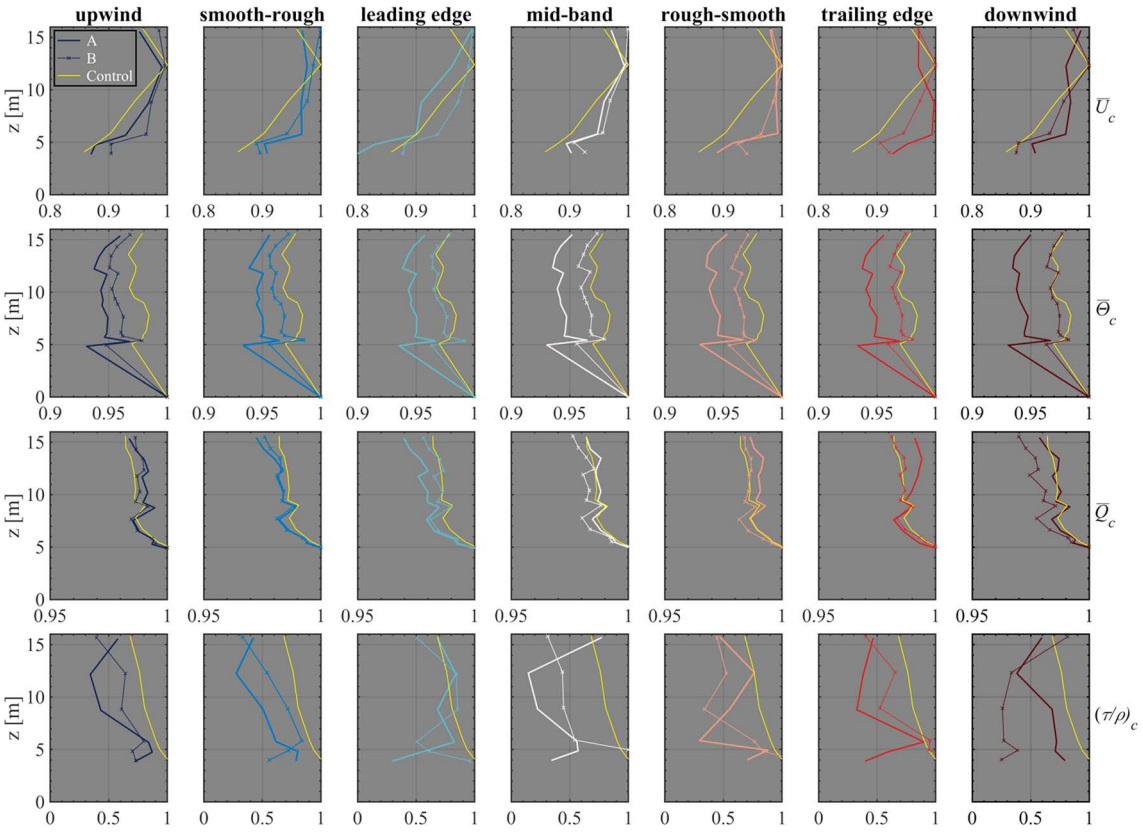

Figure 5. Profiles of marine atmospheric surface layer parameters for A and B at different times relative to nonlinear internal wave front leading edge arrival. A control profile represents conditions during the diurnal sea breeze (8 October, 01:00–02:00 UTC). See equation (3) for profile derivation and scaling.

coinciding with the arrival/departure of the NIWs. To reduce noise, an 11-min wide Savitzky-Golay filter was applied to $\overline{wu}$, which highlights this trend and revealed distinct local maxima associated with individual fronts D and E. Specifically, the momentum flux over the NIW packet was 89.7% and 61.9% higher than times immediately before and after the NIW packet arrival, respectively (see supporting information). During this time, the increased momentum flux does not coincide with a substantial change in either wind or dominant wave conditions. In Figures 4a–4c, the increased intensity near 00:00 UTC was not associated with NIWs, but rather with the commencement of the diurnal sea breeze, which preferentially impacted the along-wind momentum flux component (i.e., $\overline{wu}$).

3.3. Quasi-Instantaneous Profile Response

The quasi-instantaneous MASL response to NIW fronts A and B are given in Figure 5, for $\overline{U}_c$, $\overline{\Theta}_c$, $\overline{Q}_c$, and $(\tau/\rho)_c$ (see equation (3); for clarity the explicit z dependence is dropped). The last term is the wind stress (momentum flux) per unit density, defined using $u_*^2 = \sqrt{\overline{wu}^2 + \overline{wv}^2}$. In general, the control profile exhibited a slightly sheared wind gradient, mixed (and slightly unstable) thermodynamic structure, and relatively weak, negative stress gradient, $\partial(\tau/\rho)/\partial z < 0$. Front A resided at the ASIM ~3.5 min, with the mast being midband at ~1.75 min; for B, the front took 4.5 min to traverse the ASIM. The lowest ASIM level was not considered because of the confounding impact of surface gravity waves, and for $\overline{\Theta}_c$, the profile includes the observed SST.

$\overline{\Theta}_c$ did not exhibit any response to A or B (Figure 5). However, $\overline{Q}_c$ was more responsive to the fronts, especially for A, with the strongest response coinciding with the arrival of midband, as opposed to band edges. Relative to the control, the gradient in $\overline{Q}_c$ became progressively larger until midband, where the profile snapped back to the control. As the front moves downwind, a countergradient forms with a distinct $\overline{Q}_c$ minima at ~6 m. Once the front is completely downwind, $\overline{Q}_c$ returned to the control. This NIW-associated variance is substantial, given that Q and $\partial Q/\partial z$ are expected to vary little under typical MASL conditions.

For both A and B, the $\overline{U}_c$ adjustment was more obvious and associated with the frontal edges, that is, the smooth-rough transitions. When the fronts were upwind, $\overline{U}_c$ was very similar to the control. On approach, $\overline{U}_c$ became two-layered, with a uniform upper profile ($>$ 6 m) and a highly sheared lower layer; however, when the leading edge arrived, this two-layered flow disappeared. Over the band and as the trailing edge approached, this two-layered $\overline{U}_c$ reforms. During A, a very low-level jet formed in response to the rough-smooth transition. In both cases, $\overline{U}_c$ returned to the upwind profile as the front moved downwind.

The $(\tau/\rho)_c$ response was complex, which was expected given the high uncertainty of an individual, short Δt covariance. To contrast, the relatively smooth control profile is an average representing a significant amount of variability (see supporting information Figure S7). On approach, $(\tau/\rho)_c$ followed the control but abruptly changed when the leading edge arrived: with the upper profile ($>$ 6 m) becoming approximately uniform and then transitioning to a strongly positive stress gradient near the surface. Midband, $(\tau/\rho)_c$ was highly mixed, with multiple transition regions. As the front moved downwind, the profiles became less complex and vertically uniform. For front A, the profile approximately returned to the control, but this was not the case during B.

4. Discussion and Summary

The results of the first field-based analysis of the impact NIWs have on the MASL have been presented. While the findings of this study are noteworthy, there are some limitations that bear mentioning. As a case study, generalizing these findings is difficult, but as the principle physical interactions between NIW and the MASL have been investigated here, the results may allude to a more widely observable phenomenon. Extracting the MASL response to a single NIW is challenging, given that point measurements comprise a biased distribution of upstream variance. For example, the mixed $(\tau/\rho)_c$ response largely reflected a limitation of the eddy covariance method in this short time domain analysis, but the consistent flow adjustment observed in $\overline{U}_c$, relative to the control, demonstrated a mechanical response that implies the generation of height-dependent, atmospheric turbulence production strongly associated with NIWs. Further study using a truly controlled domain (e.g., Hao & Shen, 2018) or recently developed tools (e.g., Laxague et al., 2018) may surmount this problem and provide more fundamental insights that can be incorporated into the numerical modeling of this phenomenon.

NIWs have a distinct and significant impact on MASL variability and structure, especially for the kinematic components of the MASL flow. Spectral analysis directly linked NIW variance with corresponding responses in the mean wind speed and turbulent Reynolds stresses. The incidence of a NIW packet at *FLIP* locally enhanced the wind velocity variance throughout the MASL and drove the majority of the air-sea momentum flux. These temporal responses were distinct, but of comparable intensity, to the onset of the diurnal sea breeze after the departure of the NIW packet. This analysis also demonstrated that the MASL flow adjusts quasi-instantaneously to individual fronts. It was observed that the leading and trailing edges of a single NIW generates an internal boundary layer-like structure that exists on a much finer spatial-temporal scale than is typically conceived and which is trapped to NIW surface bands. Critical to this analysis was the ability to track these bands in space-time and sync their presence to MASL signals. In conjunction, these analyses provide compelling evidence for the interaction between a propagating internal ocean process and the MASL, across all scales associated with NIWs. While this work addresses a lingering gap in air-sea interaction study, further work is needed to better understand the distributed impact of this physical interaction and the exact mechanism by which it occurs.

Acknowledgments
This research was funded by the Office of Naval Research (ONR) Grant N0001418WX01087 under its Multidisciplinary University Research Initiative (MURI). The authors greatly appreciate the significant efforts, expertise, and geniality-under-duress of the Captain and crew of the *FLIP*, without whom this work would not have been possible. We also appreciate the efforts of all involved in the CASPER-West field work, especially those of the NPS Boundary Layer Processes group: Denny Alappattu, Alex Olson, Ben Wauer, Kyle Franklin, Anna Hook, and Richard Lind. The conceptualization and background understanding of this study benefited greatly from conversations with Sean Haney. The data used to conduct this analysis can be accessed online (https://nps.box.com/v/NPS-FLIP-internalwaves).

References

Apel, J., & Gonzalez, F. (1983). Nonlinear features of internal waves off Baja California as observed from the SEASAT imaging radar. *Journal of Geophysical Research*, *88*, 4459–4466. https://doi.org/10.1029/JC088iC07p04459

Biltoft, C. A., & Pardyjak, E. R. (2009). Spectral coherence and the statistical significance of turbulent flux computations. *Journal of Atmospheric and Oceanic Technology Notes Corresponding*, *26*, 403. https://doi.org/10.1175/2008JTECHA1141.1

Bradshaw, P., & Huang, G. P. (1995). The law of the wall in turbulent flow. *Proceedings of the Royal Society of London A*, *451*(1941), 165–188. https://doi.org/https://doi.org/10.1098/rspa.1995.0122

Brandt, P., Romeiser, R., & Rubino, A. (1999). On the determination of characteristics of the interior ocean dynamics from radar signatures of internal solitary waves. *Journal of Geophysical Research*, *104*, 30,039–30,045. https://doi.org/10.1029/1999JC900092

Charnock, H. (1955). Wind stress on a water surface. *Quarterly Journal of the Royal Meteorological Society*, *81*(350), 639–640.

Dietz, R. S., & Lafond, E. C. (1950). Natural slicks on the ocean. *Journal of Marine Research*, *9*(2), 69–76. https://apps.dtic.mil/docs/citations/ADA314074

Drennan, W. M., Taylor, P. K., & Yelland, M. J. (2005). Parameterizing the sea surface roughness. *Journal of Physical Oceanography*, *35*, 14.
Ewing, G. C. (1950). Relation between band slicks at the surface and internal waves in the sea. *Source Science New Series*, *111*(2874), 91–94.
Garrett, C., & Munk, W. (1979). Internal waves in the ocean. *Annual Review of Fluid Mechanics*, *11*, 339–69.
Gaube, P., Chickadel, C. C., Branch, R., & Jessup, A. (2019). Satellite observations of SST-induced wind speed perturbation at the oceanic submesoscale. *Geophysical Research Letters*, *46*, 2690–2695. https://doi.org/10.1029/2018GL080807
Hao, X., & Shen, L. (2018). Zebra at sea: Numerical modelling of the surface roughness induced by internal waves. *American Geophysical Union, Fall Meet. 2018, Abstr. #OS31E-1829*. Retrieved from http://adsabs.harvard.edu/abs/2018AGUFMOS31E1829H
Hsu, M.-K., & Liu, A. (2000). Nonlinear internal waves in the South China Sea. *Canandian Journal Remote Sensing*, *26*(2). https://doi.org/10.1080/07038992.2000.10874757
Hultmark, M., Calaf, M., Parlange, M. B., Hultmark, M., Calaf, M., & Parlange, M. B. (2013). A new wall shear stress model for atmospheric boundary layer simulations. *Journal of the Atmospheric Sciences*, *70*(11), 3460–3470. https://doi.org/10.1175/JAS-D-12-0257.1
Hwang, P. A. (2005). Wave number spectrum and mean square slope of intermediate-scale ocean surface waves. *Journal of Geophysical Research*, *110*, C10029. https://doi.org/10.1029/2005JC003002
Jiménez, P. A., & Dudhia, J. (2018). On the need to modify the sea surface roughness formulation over shallow waters. *Journal of Applied Meteorology and Climatology*, *57*(5), 1101–1110. https://doi.org/10.1175/JAMC-D-17-0137.1
Jones, I. S., Volkov, Y. A., Toba, Y., Larsen, S., & Huang, N. (2001). Overview. In I. S. Jones, & Y. Toba (Eds.), *Wind stress over the ocean 307*. Cambridge: Cambridge University Press.
Kitaigorodskii, S., & Volkov, Y. A. (1965). On the roughness parameter of the sea surface and the calculation of momentum rlux in the near-water layer of the atmosphere. *Izvestiya, Atmospheric and Oceanic Physics*, *1*, 973–988.
Lamb, K. G. (2014). Internal wave breaking and dissipation mechanisms on the continental slope/shelf. *Annual Review of Fluid Mechanics*, *46*(1), 231–254. https://doi.org/10.1146/annurev-fluid-011212-140701
Laxague, N. J. M., Haus, B. K., Bogucki, D., & Özgökmen, T. (2015). Spectral characterization of fine-scale wind waves using shipboard optical polarimetry. *Journal of Geophysical Research: Oceans*, *120*, 3140–3156. https://doi.org/10.1002/2014JC010403
Laxague, N., Haus, B., Ortiz-Suslow, D., & Graber, H. (2018). Quantifying highly variable air-sea momentum flux using wavelet analysis. *Journal of Atmospheric and Oceanic Technology*, *35*, 15.
MacKinnon, J. A., & Gregg, M. C. (2005). Spring mixing: Turbulence and internal waves during restratification on the New England shelf. *Journal of Physical Oceanography*, *35*(12), 2425–2443. https://doi.org/10.1175/JPO2821.1
MacMahan, J. (2017). Increased aerodynamic roughness owing to surfzone foam. *Journal of Physical Oceanography*, *47*(8), 2115–2122. https://doi.org/10.1175/JPO-D-17-0054.1
National Geophysical Data Center, N. (2016). U.S. coastal relief model—Southern California. https://doi.org/doi:10.7289/V500001J
Ortiz-Suslow, D. G., Haus, B. K., Williams, N. J., Graber, H. C., & MacMahan, J. H. (2018). Observations of air-sea momentum flux variability across the inner shelf. *Journal of Geophysical Research: Oceans*, *123*, 8970–8993. https://doi.org/10.1029/2018JC014348
Ortiz-Suslow, D. G., Haus, B. K., Williams, N. J., Laxague, N. J. M., Reniers, A. J. H. M., & Graber, H. C. (2015). The spatial-temporal variability of air-sea momentum fluxes observed at a tidal inlet. *Journal of Geophysical Research: Oceans*, *120*, 660–676. https://doi.org/10.1002/2014JC010412
Ortiz-Suslow, D. G., Kalogiros, J., Yamaguchi, R., Alappattu, D., Franklin, K., Wauer, B., & Wang, Q. (2019). The data processing and quality control of the marine atmospheric boundary layer measurement systems deployed by the Naval Postgraduate School during the CASPER-West field campaign (Tech. Rep). Monterey, CA: Naval Postgraduate School. https://doi.org/NPS-MR-19-001
Ortiz-Suslow, D. G., Wang, Q., Kalogiros, J., Yamaguchi, R., Celona, S., de Paolo, T., et al. (2019). Quantifying the impact of nonlinear internal waves on the marine atmospheric surface layer. In *2019 IEEE/OES twelfth current, waves and turbulence measurement and applications*. San Diego: IEEE.
Phillips, O. (1980). *The dynamics of the upper ocean* (2nd ed.). Cambridge: Cambridge University Press.
Prandtl, L. (1925). Bericht über Untersuchungen zur ausgebildeten Turbulenz. *Zeitschrift für Angewandte Mathematik und Mechanik*, *5*(2), 136–139.
Wang Q., Alappattu D. P., Billingsley, S., Blomquist, B., Burkholder, R. J., Christman, A. J., et al. (2018). CASPER: Coupled Air-SeaProcesses and Electromagnetic (EM) Wave ducting Research. *Bulletin of the American Meteorological Society 99*(7), 1449–1471. https://doi.org/10.1175/BAMS-D-16-0046.1
Wenegrat, J. O., & Arthur, R. S. (2018). Response of the atmospheric boundary layer to submesoscale sea surface temperature fronts. *Geophysical Research Letters*, *45*, 13,505–13,512. https://doi.org/10.1029/2018GL081034
Woodcock, A. H., & Wyman, J. (1947). Convective motion in air over the sea. *Annals of the New York Academy of Sciences*, *48*(8), 749–776. https://doi.org/10.1111/j.1749-6632.1947.tb38488.x
Zhang, F. W., Drennan, W. M., Haus, B. K., & Graber, H. C. (2009). On wind-wave-current interactions during the Shoaling Waves Experiment. *Journal of Geophysical Research*, *114*, C01018. https://doi.org/10.1029/2008jc004998
Zhang, J. A., Katsaros, K. B., Black, P. G., Lehner, S., French, J. R., & Drennan, W. M. (2008). Effects of roll vortices on turbulent fluxes in the hurricane boundary layer. *Boundary-Layer Meteorology*, *128*(2), 173–189. https://doi.org/10.1007/s10546-008-9281-2